High-pressure phase of $CrSb_2$: A new quasi-one-dimensional itinerant magnet with competing interactions

Y. Y. Jiao,[1,2,3=] Z. Y. Liu,[1,4=] M. A. McGuire,[5] S. Calder,[6] J.-Q. Yan,[5] B. C. Sales,[5] J. P. Sun,[1,7] Q. Cui,[1,7] N. N. Wang,[1,7] Y. Sui,[4] Y. Uwatoko,[8] B. S. Wang,[1,7,9] X. L. Dong,[1,7,9] Z. X. Zhao,[1,7,9] and J.-G. Cheng[1,7,9*]

[1]*Beijing National Laboratory for Condensed Matter Physics and Institute of Physics, Chinese Academy of Sciences, Beijing 100190, China*

[2]*The State Key Laboratory of Refractories and Metallury, Wuhan University of Science and Technology, Wuhan, Hubei 430081, China*

[3]*Faculty of Science, Wuhan University of Science and Technology, Wuhan, Hubei 430062, China*

[4]*Department of Physics, Harbin Institute of Technology, Harbin 150001, China*

[5]*Materials Science and Technology Division, Oak Ridge National Laboratory, Oak Ridge, Tennessee 37831, USA*

[6]*Neutron Scattering Division, Oak Ridge National Laboratory, Tennessee 37831, USA*

[7]*School of Physical Sciences, University of Chinese Academy of Sciences, Beijing 100190, China*

[8]*Institute for Solid State Physics, University of Tokyo, Kashiwa, Chiba 277-8581, Japan*

[9]*Songshan Lake Materials Laboratory, Dongguan, Guangdong 523808, People's Republic of China*

= These two authors contributed equally to this work.
*E-mail: jgcheng@iphy.ac.cn

Abstract

We have synthesized the high-pressure form of $CrSb_2$ with $CuAl_2$-type structure under 7 GPa and 700 °C, and characterized its structural, transport, and magnetic properties by a suite of measurement techniques over a broad range of temperature, magnetic field, and pressure. In addition to previously reported ferromagnetic (FM) transition at $T_C \approx 160$ K, we discover another antiferromagnetic spin-density-wave (SDW) transition at $T_s \approx 90$ K, which is characterized by FM sheets of spins in the *ab* plane that vary along the *c*-axis as determined by neutron powered diffraction. Pronounced anomalies around these two magnetic transitions are visible only in the lattice parameter *c*, singling a strong spin-lattice coupling along the -Cr-Cr-Cr- infinite linear chains. We find that the application of magnetic field can suppress the SDW phase and stabilize the FM state down to the lowest temperature above $\mu_0 H_c \approx 3$ T, around which a peculiar non-Fermi-liquid behavior with reduced effective mass emerges. On the other hand, the application of high pressure induces complex evolution of the magnetic states, i.e. the FM order is lowered while the SDW order is enhanced quickly until they merge together into a single antiferromagnetic transition, which is suppressed completely at $P_c \approx 9$ GPa. We observe near P_c non-Fermi-liquid behavior and enhancement of effective mass, which are hallmarks of magnetic quantum criticality. No superconductivity was observed down to 2 K around P_c.

Keywords: $CrSb_2$, high-pressure synthesis, itinerant-electron ferromagnet

Introduction

The 3d transition-metal diantimonides (MSb$_2$) exhibit interesting structural and physical properties. [1, 2] In terms of the crystal structure, MSb$_2$ can be divided into two groups: the arsenopyrite-type (or CuAl$_2$-type) tetragonal structure with space group *I4*/*mcm* (No. 140) for M = Ti and V, and the marcasite-type orthorhombic structure with space group *Pnnm* (No. 58) for M = Cr, Mn, Fe, Co, Ni. The former has a high coordination number while the latter has a low coordination number around the M atom. In the CuAl$_2$-type structure, each M atom is surrounded by 8 Sb atoms at equal distance, and the MSb$_8$ decahedra share faces to form an infinite linear -M-M-M- chain along the c-axis. [3] In contrast, the M cations are octahedrally coordinated by 6 Sb atoms, forming the low-coordination group, for the late transition-metal MSb$_2$ with marcasite-type structure.[1]

For TiSb$_2$ and VSb$_2$ with CuAl$_2$-type structure, similar paramagnetic and metallic behaviors were observed.[4] But marcasite-type MSb$_2$ compounds display distinct magnetic and electronic ground states. Both FeSb$_2$ and CrSb$_2$ are well-known narrow-gap semiconductors with intriguing physical properties as a manifestation of strong electron-electron correlations in the narrow 3d bands.[5-7] Long-range antiferromagnetic (AF) order is formed at the Néel temperature T_N = 273 K in CrSb$_2$,[6] while a crossover from low-temperature diamagnetism to enhanced paramagnetism takes place around 150 K in FeSb$_2$.[8] CoSb$_2$ also exhibits a semiconducting behavior and has been considered as a potential thermoelectric material.[9] In contrast to the above thermodynamically stable compounds at ambient pressure, MnSb$_2$ with marcasite-type structure can only be obtained under moderate high-pressure and high-temperature (HPHT) conditions, e.g. 6 GPa and 650 °C.[10] The physical properties of MnSb$_2$ remains largely unknown so far.

It has been argued that the crystal structure of binary MSb$_2$ depends on the ionic radius of M cation, and the adoption of CuAl$_2$-type structure in TiSb$_2$ and VSb$_2$ was attributed to the relatively large size of the transition-metal atoms.[4] Since CrSb$_2$ is located at the boundary dividing the low- and high-coordination groups, Takizawa *et al*. [11] prepared a high-pressure polymorph of CrSb$_2$ with CuAl$_2$-type structure at pressure (P) over 5.5 GPa and temperature (T) 500-700 °C. As mentioned above, the high-pressure form is featured by -Cr-Cr-Cr- infinite chains along the c-axis with metallic bond nature. Different structures usually offer distinct electronic ground states. In contrast to the AF semiconducting ground state for marcasite-type CrSb$_2$,[6] the CuAl$_2$-type CrSb$_2$ was found to be an itinerant-electron ferromagnet with a Curie temperature $T_C \approx 160$ K.[11] The saturation moment was found to be ~1.2 μ_B/Cr, which is about half of the effective paramagnetic moment of 2.5 μ_B/Cr, characteristic of itinerant-electron magnetism.[12, 13] The resistivity $\rho(T)$ was found to exhibit a hump anomaly around T_C. In the earlier study by Takizawa *et al*.,[11] the physical properties of CuAl$_2$-type CrSb$_2$ were measured from room temperature down to ~77 K, and no further studies were reported on this interesting itinerant-electron ferromagnet so far to our knowledge.

In this work, we have reinvestigated the high-pressure form of CrSb$_2$ synthesized under 7 GPa and 700 °C. Below the previously reported ferromagnetic (FM) transition at $T_C \approx 160$ K, we observe another AF spin-density-wave (SDW) transition at $T_s \approx 90$ K. We determined the magnetic spin structures by means of neutron powder diffraction and studied the spin-lattice coupling with low-temperature X-ray

diffraction. In addition, we have also studied the effects of external magnetic field and physical pressure on the magnetic and transport properties of $CrSb_2$ in the context of magnetic quantum criticality. While the external magnetic field can stabilize the FM state above $\mu_0 H_c \approx 3$ T, the application of high pressure induces complex evolution of the magnetic states and realizes an AF quantum critical point around $P_c \approx 9$ GPa.

Experimental Details

We used either pulverized single crystal or polycrystalline $CrSb_2$ samples with marcasite-type structure as the precursor for HPHT syntheses. The single crystals of $CrSb_2$ were grown out of the Sb flux as described elsewhere,[6] while the polycrystalline samples were obtained by reacting a stoichiometric mixture of high-purity Cr and Sb powders in a vacuum-sealed quartz ampoule at 680 °C for 20 h and then 1000 °C for 20 h. The HPHT syntheses in the present study were performed with a Kawai-type multianvil module (Max Voggenreiter GmbH) in the Institute of Physics, CAS. Semi-sintered octahedron made of Ceramacast 584-OF is used as the pressure medium, and the graphite sleeve serves as heater. The precursor was encapsulated in the h-BN crucible and then subjected to HPHT treatment at 7 GPa and 700 °C for 30 min. The temperature was quenched to room temperature before releasing pressure slowly. The sample was finally recovered and subjected to various measurements of physical properties at ambient or high pressures.

Phase purity of the obtained samples was examined at room temperature with powder X-ray diffraction (XRD). Structural parameters were extracted from the XRD patterns via Rietveld refinement with the FullProf program. Low-temperature XRD data in the temperature range 20-300 K were collected with a PANalytial X'pert Pro MPD diffractometer and Oxford PheniX cryostat. Neutron powder diffraction (NPD) was carried out on the HB-2A diffractometer at the High Flux Isotope Reactor (HFIR), Oak Ridge National Laboratory. A wavelength of $\lambda = 2.41$ Å was selected using the 113 reflection of a germanium monochromator. The sample was loaded into an aluminum sample can and the temperature controlled using a ^{4}He cryostat in the temperature range 1.5-300 K. A 2θ scattering range of 3-130° was covered in 0.05° step size. The data was collected using 44 ^{3}He detectors.

DC magnetic susceptibility under different magnetic fields and isothermal magnetization at different temperatures were measured with a commercial Magnetic Property Measurement System (MPMS-III, Quantum Design). Measurements of resistivity with standard four-probe configuration and specific heat with two-tau relaxation method were carried out by using the Physical Property Measurement System (PPMS, Quantum Design). Thermopower was measured with the steady-state method in a home-made setup.[14] DC magnetic susceptibility under different hydrostatic pressures up to 0.9 GPa was measured with a miniature piston-cylinder cell (PCC) in MPMS. We also measured ac magnetic susceptibility with mutual induction method in a self-clamped PCC up to 1.5 GPa. For both cases, the sample together with a piece of lead (Pb) were loaded into a Teflon cell filled with Daphne 7373 as the pressure transmitting medium (PTM). The pressure values inside the PCC were determined from the superconducting transition temperature of Pb. The resistivity under different hydrostatic pressures up to 11 GPa was measured with a palm cubic anvil cell (CAC) apparatus.[15] Glycerol was used as the PTM for CAC and the pressure was estimated from the force-pressure calibration curve at room temperature.

Results and Discussions

1. Structural characterization

Figure 1 shows the powder XRD pattern of $CrSb_2$ prepared at 7 GPa and 700 °C. It confirms that the as-obtained sample is single phase with body-centered tetragonal structure. We performed the Rietveld refinement on the XRD pattern by taking the $CuAl_2$-type structure model defined in space group *I4/mcm* with the Cr atom at *4a* (*0,0,1/4*) and the Sb atom at *8h* (*x,y,0*) site. As illustrated in Fig. 1, the refinement converged well with small reliability factors of $R_p = 2.45\%$, $R_{wp} = 3.13\%$, and $\chi^2 = 1.38$. The obtained lattice parameters $a = 6.4904(2)$ Å and $c = 5.7459(2)$ Å are in excellent agreement with those reported by Takizawa *et al*.[11]

As illustrated in the inset of Fig. 1, the crystal structure of $CuAl_2$-type $CrSb_2$ is featured by face-shared $CrSb_8$ decahedral chains along the *c*-axis. Each Cr atom is surrounded by eight Sb atoms at equal distance of 2.836(1) Å to form a $CrSb_8$ decahedron, which shares square faces with each other along the *c*-axis, forming an infinite $CrSb_8$ decahedral chain with the nearest-neighbor Cr-Cr distance of 2.873(1) Å. These $CrSb_8$ decahedral chains are interconnected with each via sharing common edges within the *ab* plane. Since the Cr-Cr distance of 4.589 Å across the common edge within the *ab* plane is much longer than that of 2.873 Å across the common face along the *c*-axis, the high-pressure $CuAl_2$-type $CrSb_2$ can be considered as a quasi-one-dimensional (Q1D) compound.

As mentioned by Takizawa *et al.*,[11] the high-pressure $CuAl_2$-type $CrSb_2$ is metastable at ambient condition, and transforms to low-pressure marcasite-type phase when heated above 300 °C at ambient pressure. We noticed that the high-pressure phase can transform slowly to low-pressure phase even at room temperature whether stored in air or Ar-filled glove box. In order to measure the physical properties on freshly made samples, we therefore synthesized several batches of $CrSb_2$ samples labeled as S1 to S4 under similar HPHT conditions during the courses of physical properties measurements. As illustrated in Figs. S1 and S2 of Supplementary Materials, their XRD patterns and lattice parameters are nearly identical, whereas their physical properties display some variations, though the essential characteristics are very similar. Thus, in the following we specified on which sample the physical properties were measured.

2. Physical properties at ambient pressure

Figure 2 summarizes the physical properties of high-pressure phase of $CrSb_2$. Two characteristic phase transitions are marked by the vertical dotted lines. Fig. 2(a) shows the temperature dependence of the dc magnetic susceptibility $\chi(T)$ measured upon warming up after zero-field-cooled (ZFC) and field-cooled (FC) from room temperature under an external magnetic field of $\mu_0 H = 0.1$ T. As can be seen, ZFC/FC $\chi(T)$ curves overlap with each other and both exhibit a quick increase below ~160 K, corresponding to the paramagnetic (PM) to FM transition as reported previously.[11] Then, the $\chi(T)$ curves experience a quick drop below ~ 100 K, signaling the transition to an AF SDW state as determined below, which was not reported in the previous study.[11] From the peaks of $d\chi/dT$, we can determine the FM and SDW transition temperatures as $T_C^{\chi} = 159$ K and $T_s^{\chi} = 88$ K, respectively. The inverse magnetic susceptibility $\chi^{-1}(T)$ shown in Fig. 2(a) displays an obvious upward deviation from the Curie-Weiss (CW) behavior upon approaching T_C from above in the PM region, implying the presence of strong critical spin fluctuations. A CW fitting to $\chi^{-1}(T)$ in the linear region between 250 and 300 K yields an effective moment of $\mu_{eff} = 3.33\ \mu_B$/f.u.

and the CW temperature of θ_{cw} = 198 K. The positive θ_{cw} signals dominant FM interactions in this compound. According to the NPD refinements and isothermal $M(H)$ curve shown below, the saturation moment of $CrSb_2$ is about 1.3 μ_B, much smaller than μ_{eff}, in line with the scenario of itinerant-electron magnetism.[12, 13]

Temperature dependence of resistivity $\rho(T)$ shown in Fig. 2(b) confirms a metallic behavior for $CrSb_2$ over the whole temperature range with two distinct anomalies near the magnetic transitions. This can be seen clearly from the temperature derivative of resistivity, $d\rho/dT$, shown in Fig. 2(b). The kink-like anomaly in $\rho(T)$ at T_C, corresponding to a λ-shaped anomaly in $d\rho/dT$, should be ascribed to the reduction of magnetic scattering upon the formation of long-range FM order. On the other hand, the hump anomaly in $\rho(T)$ around T_s manifested by a sharp dip in $d\rho/dT$ should be attributed to the formation of SDW order that gaps partially the density of states at Fermi level. These observations not only demonstrate a strong interplay between the spin and charge degrees of freedom in this system, but also further underline the itinerant-electron character of this magnetic system. It should be noted that the transition temperatures, T_C^{ρ} = 156 K and T_s^{ρ} = 86 K in Fig. 2(b), determined from $d\rho/dT$ is slight lower than those defined from $\chi(T)$.

The metallic character and magnetic orderings in $CrSb_2$ are also evidenced by the specific heat $C(T)$ data shown in Fig. 2(c). A weak peak anomaly in $C(T)$ around T_C confirms the bulk nature of the FM transition. It should be noted that the $C(T)$ peak appears at a temperature ~ 10 K below T_C determined from $\chi(T)$ and $\rho(T)$, presumably due to the sample dependent issue or the polycrystalline nature for the studied sample. In contrast, no obvious $C(T)$ anomaly can be discerned around T_s, except for a quite broad hump superimposed on a smooth lattice background. This may become visible if the lattice contribution can be subtracted properly. The inset of Fig. 2(c) shows the low-temperature $C(T)$ data in the form of C/T versus T^2, which exhibits a nice linear behavior below 12 K. From the linear fitting shown as the solid line, we obtained the electronic Sommerfeld coefficient γ = 17.3 mJ/mol-K^2, β = 0.4343 mJ/mol-K^4. The finite γ value confirms the metallic ground state and the Debye temperature θ_D = 237 K can be obtained according to $\theta_D = \left(12\pi^4 nR/5\beta\right)^{1/3}$, Where R is the ideal gas constant, n = 3 is the number of atoms per formula unit.

Figure 2(d) depicts the thermopower $S(T)$ of $CrSb_2$, from which we can gain further information about the charge carriers. As can be seen, the negative $S(T)$ signals a dominant n-type charge carries in this compound and the quite small magnitude of $|S(T)|$ is consistent with the metallic behavior seen in $\rho(T)$. The strong coupling between the spin and charge degrees of freedom causes an obvious inflection point of $S(T)$ at T_C as shown in Fig. 2(d), while it is hard to discern any anomaly around T_s in $S(T)$. Although the gradual formation of SDW should gap partially the density of states at Fermi level, resulting in a humplike anomaly in $\rho(T)$ at T_s, the gradual change of density of states should have an insignificant impact on the $S(T)$ because thermopower is proportional to the energy derivative of the density of states at Fermi level. As such, the anomaly of $S(T)$ at T_s is quite weak.

From these above characterizations, we can conclude that the high-pressure

$CuAl_2$-type $CrSb_2$ is an itinerant-electron magnet that undergoes two successive magnetic transitions at $T_C \approx 160$ K and $T_s \approx 90$ K, respectively. The former is a PM to FM transition manifested by obvious anomalies in resistivity, thermopower, and specific heat due to the presence of strong critical scattering. The latter should be ascribed to a transition from FM to an AF, most likely SDW type magnetic order, which opens gap on part of the Fermi surfaces so as to induce a hump anomaly in resistivity as observed in Cr metal.[16] These observed phenomena in $CuAl_2$-type $CrSb_2$ are very similar with those of helimagnetic MnP,[17] and suggests the presence of competing FM and AF exchange interactions. In comparison with the previous study by Takizawa *et al.*,[11] we not only provide more evidences for the bulk FM transition at T_C, but also uncover a new AF SDW type magnetic transition at T_s, thus offering a new material platform for studying the rich physics of itinerant-electron magnetism.

3. Magnetic structures

NPD was performed to determine the magnetic structures of $CrSb_2$. Refinements of NPD patterns from 180 down to 2K evidenced no structural phase transition and all data can be described in the *I4/mcm* space group. As shown in Fig. 3(a), measurements from 180 to 120 K revealed the onset of magnetic ordering with the development of a peak around $2\theta = 30.5°$ ($|Q| = 1.37$ Å^{-1}), consistent with FM ordering at 160 K. This could be indexed to a $\mathbf{k} = (0,0,0)$ propagation vector. To determine the magnetic structure a representational analysis approach was performed with the SARAh software.[18] With the Cr atom at *4a* (*0,0,1/4*) in Kovalev's scheme this yielded symmetry allowed irreducible representations, with only Γ_3 and Γ_9, producing scattering at the position corresponding to the magnetic reflections. Γ_3 corresponds to FM ordering along the *c*-axis while Γ_9 corresponds to FM ordering in the *ab* plane. While the data did not allow an unambiguous distinction, we assign the most likely magnetic structure for this intermediate FM phase to that with spins confined in the *ab* plane (Γ_9), as shown in Fig. 3(b). The ordered moment at 120 K is 0.87(6) μ_B/Cr. This description of the magnetic structure is driven by the evolution of the magnetism below 120 K, discussed below, which can only be described by a single magnetic structure. However, we cannot rule out small canting along the *c*-axis with the present data for the FM phase.

Upon cooling below 120 K, NPD data reveal the development of magnetic scattering at low angles, Fig. 3(c). This peak shifts in position and is tracked by a shifting of the observed reflection from the FM phase, which is located at $2\theta = 30.5°$ ($|Q|$=1.37 Å^{-1}) at 120 K. The peak shifting is much stronger than the change in crystal structure reflections and thus indicates an alteration of the propagation vector from (0,0,0) to an incommensurate one. The onset temperature of this peak corresponds to the transition observed in magnetic susceptibility and resistivity. While it is challenging to determine uniquely the value of the incommensurate propagation vector from NPD, the anomalies found in the crystal structure along the *c*-axis below led us to consider an alteration of the propagation in the form (0,0,δ). We additionally considered propagation vector (δ,δ,0) and (δ,δ,δ), which, however, did not produce reasonable results. We are able to index the reflections at 105 K using k = (0,0,0.1). Upon cooling, this alters to k = (0,0,0.16) at 90 K and continues shifting to k = (0,0,0.22) at the lowest measured temperature of 2 K. Only the Γ_9 irreducible representation with spins in the *ab* plane can model the data, so we are able to uniquely define the low-temperature magnetic structure, shown in Fig. 3(d). This corresponds to the magnetic space group $C_A mca$ (#63.468) in BNS notation. The magnetic structure is

indeed an SDW with FM sheets of spins in the *ab* plane that alter in magnitude and direction throughout the unit cell. The fully ordered moment is 1.21(8) μ_B/Cr at 2 K.

4. Low-temperature XRD

To investigate the structural responses at the magnetic transitions, we measured low-temperature XRD, which evidenced significant anisotropic lattice changes across these two magnetic transitions. Figure 4(a) depicts the variations with temperature of the lattice parameters *a* and *c* in the temperature range from 300 down to 20 K. As can be seen, the tetragonal *a* (= *b*) axis displays a smooth and continuous normal contraction upon cooling, whereas the *c*-axis first experiences an anomalous expansion at T_C and then a quick contraction below T_s. The observations of first expansion at T_C and then contraction at T_s are consistent with the general expectations for parallel and then antiparallel alignment of spins in the 1D -Cr-Cr-Cr- chains running along the *c*-axis. As a result, the *c*/*a* ratio displays corresponding anomalies at T_C and T_s, and the unit-cell volume *V* exhibits a broad hump in the temperature region between T_s and T_C, as seen in Fig. 4(b). The anisotropic changes of lattice parameters can also be seen clearly from the intensity maps of the 420 and 004 Bragg peaks measured every 5 K on cooling from 250 to 20 K as illustrated in Figs. 4(c, d). Although the sudden shift of the 004 inflection around 90 K is indicative of first-order nature for the SDW transition, there is no extra reflections observed and the SDW order should be accompanied with an isostructural phase transition as observed in CrAs. Thus, these low-temperature structural characteristics evidenced not only strong spin-lattice coupling but also a pronounced Q1D character for the magnetic interactions in the high-pressure $CuAl_2$-type $CrSb_2$. It has been shown that the magnetic excitations of the marcasite-type $CrSb_2$ studied with inelastic neutron scattering are consistent with Q1D magnetism.[19] Thus, measurements of inelastic neutron scattering on $CuAl_2$-type $CrSb_2$ are also desirable to further elaborate the Q1D character of itinerant-electron magnetism.

5. Effect of magnetic fields

As mentioned above, the transition from FM to SDW state in $CrSb_2$ is similar to the case of MnP and signals the competition between FM and AF interactions, which can usually be tuned by external magnetic fields.[20, 21] We thus investigate the effect of magnetic field on the magnetic and transport properties of $CrSb_2$. Figure 5(a) displays the ZFC/FC $M(T)$ curves of $CrSb_2$ under various magnetic fields. The origin for the bifurcation of ZFC/FC $M(T)$ curves at $H \leq 3$ T is unclear. With increasing magnetic field, the FM transition gradually shifts to higher temperatures, whereas the SDW order is suppressed progressively and eventually converted to the FM state at 7 T. The field-induced crossover from SDW to FM state is also evidenced from the $M(H)$ curves at $T < T_s$ as shown in Fig. 5(b). At 2 K, a steep increase of $M(H)$ takes place between 1 and 4 T, and the saturation magnetic moment of $CrSb_2$ reaches ~ 1.3 μ_B, in line with the above NPD refinement. In the temperature range $T_s < T < T_C$, the $M(H)$ curves displays typical FM behavior as expected.

Since the field-induced SDW to FM transition can be regarded as a quantum phase transition (QPT) at zero temperature,[22] it is interesting to investigate its influence on the electrical transport properties across the transition. Figure 6(a) shows the $\rho(T)$ curves under various magnetic fields. In accordance with the $M(T)$ data shown in Fig. 5(a), the kink-like anomaly at T_C moves to higher temperature with increasing magnetic field, while the hump anomaly at T_s shifts to lower temperatures until it

vanishes completely around 3 T. The field dependencies of T_C and T_s determined from the dρ/dT curves in Fig. 6(a) are depicted in Fig. 7(a), which illustrates clearly an opposite field dependences and the possible occurrence of QPT from SDW to FM order with a critical point at $\mu_0 H_c \approx 3$ T.

Such a QPT is distinct from the well-studied transition from a magnetically ordered to disordered state.[23] It is thus interesting to examine whether the quantum critical fluctuations could influence the evolution of electronic quasiparticles across the field-induced QPT. For this purpose, we first fitted the low-temperature $\rho(T)$ data with a power-law formula: $\rho(T) = \rho_0 + BT^{\alpha}$, which is shown by the dotted curves in Fig. 6(a). As shown in Fig. 7(a), the obtained exponent α decreases quickly from 2.4 at 0 T to ~ 1.5 at 2.5 T, and then restores back to 2.3 at 7 T, thus evidencing a pronounced non-Fermi-liquid (nFL) behavior around 2.5 T where the QPT from SDW to FM takes place.

To evaluate the effective mass of charge carriers, we have re-plotted the low-temperature $\rho(T)$ data in the form of ρ versus T^2 in Fig. 6(b). In the same temperature range from 2 to 30 K, a clear deviation from the linear Fermi-liquid (FL) behavior is indeed confirmed for $\mu_0 H = 2$ and 2.5 T near QPT, while the FL behavior is preserved inside both SDW and FM regimes. A linear fitting was applied in the low-temperature region of Fig. 6(b) to extract the residual resistivity ρ_0 and the T-quadratic coefficient A according to $\rho(T) = \rho_0 + AT^2$. The obtained ρ_0 and A are displayed in Fig. 7(b) as a function of magnetic field. As can be seen, the coefficient A related to the effective mass of charge carriers via $A \propto (m^*/m_0)^2$ displays a sharp dip rather than a cusp across the QPT, where ρ_0 experiences a steep decrease and then tends to level off. The observed reduction of effective mass in the presence of nFL behavior near the field-induced SDW to FM QPT at $\mu_0 H_c = 2.5$ T is in sharp contrast with the general observation of divergent behavior near a QPT associated with an AF to PM transition.[23] Whether this is a generic behavior deserves further studies. The reduction of ρ_0 with field should be ascribed to the enhancement of density of states at Fermi level due to the elimination of SDW gap by magnetic field.

6. **Effect of pressure**

As a new itinerant-electron magnet, it is also interesting to investigate whether pressure can suppress the magnetic orders and/or induce superconductivity near a magnetic quantum critical point as recently found in CrAs and MnP.[24, 25] For this purpose, we first study the pressure effect on magnetic susceptibility. Figure 8(a) displays the temperature dependence of magnetization $M(T)$ for $CrSb_2$ under various pressures up to 0.9 GPa, measured with a miniature PCC in MPMS. The data were collected upon warming up under an external magnetic field of $\mu_0 H = 0.1$ T. From the temperature derivative dM/dT cures in Fig. 8(b), we can clearly see that T_C decreases while T_s increases until they merge together at $P > 0.5$ GPa. Meanwhile, the magnitude of magnetization decreases quickly and there left a single anomaly in $M(T)$, which indicates that pressure favors an AF state in $CrSb_2$. The stabilization of AF state under pressure is also consistent with the $M(H)$ data shown in Fig. 8(c), from which we can see that the critical field for metamagnetic transition increases sharply to over 5 T under 0.9 GPa. From ac magnetic susceptibility $\chi'(T)$ shown in Fig. 8(d), we can see that the spontaneous FM component disappears completely above 1.3 GPa, and $CrSb_2$ should adopt an AF state upon cooling down. From these characterizations, we can conclude that the application of high pressure suppresses the

FM order while enhances the SDW order until they merge together into a single AF transition above ~ 0.5 GPa. As shown below, the resistivity exhibits a kink anomaly at the AF transition, which is different from the hump anomaly seen around T_s. We thus labelled the emergent AF transition temperature as T_N in order to distinguish it from the low-pressure SDW transition. The exact form of this AF order remains to be determined by techniques such as high-pressure neutron diffraction.

Because the AF order with small net moment is hard to detect with mutual induction method using the self-wound coils, we resorted to high-pressure resistivity measurements to further track its variation with pressure at higher pressures. Figure 9 shows the $\rho(T)$ curves of $CrSb_2$ under various pressures up to 1.86 GPa measured with a self-clamped PCC. We also use the anomalies in $d\rho/dT$ to define the magnetic transition temperatures. As can be seen, at 0.36 GPa, T_C decreases to ~130 K while T_s increases to ~100 K, and there left a single anomaly in resistivity at 0.71 GPa, which are in excellent agreement with the high-pressure magnetic results shown in Fig. 8. Above 0.7 GPa, the kink-like anomaly at T_N moves to lower temperature gradually with increasing pressure, and it decreases to about 115 K at 1.86 GPa.

For higher pressures, we employed a CAC apparatus to track the emergent AF transition up to 11 GPa. Figure 10 displays the high-pressure $\rho(T)$ results for two $CrSb_2$ samples. From the $d\rho/dT$ curves, we can see that the AF order manifested by the kink-like resistivity anomaly is continuously suppressed to lower temperatures and vanishes completely around $P_c \approx 9$ GPa, above which no obvious anomaly can be detected in resistivity curve. This observation indicated that we should achieve a pressure-induced AF quantum critical point.

To search for evidences of quantum criticality, we performed similar analysis on the low-temperature $\rho(T)$ data as done above in Fig. 6. The obtained resistivity exponent α and the T-quadratic coefficient A as a function of pressure are displayed in Fig. 11(b). It was found that the FL behavior ($\alpha = 2$) is retained in large pressure regime under $P \leq 9$ GPa, while a nFL behavior ($\alpha \approx 1.6$) appears at 11 GPa. On the other hand, the coefficient A increases monotonically with pressure, but the divergent behavior is not very obvious. The observations indicated that the strongest critical fluctuations associated with the AF quantum critical point might be achieved at slightly higher pressure than 11 GPa.

Based on the above high-pressure measurements, we can construct a T-P phase diagram for $CrSb_2$ as shown in Fig. 11(a), which displays a rich evolution of the magnetic phases as a function of pressure. At ambient pressure, $CrSb_2$ undergoes a FM transition at $T_C \approx 160$ K followed by another transition to an incommensurate SDW state at $T_s \approx 90$ K. With increasing pressure, the FM transition is lowered while the SDW order moves up quickly until they coincide around 0.5 GPa, above which a new, single AF order is formed below T_N. This AF order can be eliminated completely at $P_c \geq 9$ GPa.

Such an evolution of magnetic ground states with pressure is very similar with that of MnP, featured by competing FM and AF interactions. Unfortunately, we did not observe pressure-induced superconductivity near P_c down to 2 K, even though hallmarks of quantum criticality are seen near P_c. Since the superconductivity of MnP was observed around 1 K in high-quality single crystal samples,[25] it deserves further explorations, especially to perform high-pressure measurements on high-quality single-crystal samples of $CrSb_2$ to much lower temperatures.

Conclusion

We have synthesized the high-pressure form of $CrSb_2$ with $CuAl_2$-type structure, and characterized its structural, transport and magnetic properties over a broad range of temperature, magnetic field, and pressure. We discover a new SDW transition at $T_s \approx$ 90 K below the previously reported FM transition at $T_C \approx 160$ K. Pronounced anomalies only in the lattice parameter *c* around these two magnetic transitions signal a strong spin-lattice coupling within the Q1D -Cr-Cr-Cr- infinite chains. We also manipulated the competition between FM and AF interactions in $CrSb_2$ by applying external magnetic field and physical pressure. It was found that the application of magnetic field can suppress the SDW state and stabilize the FM state down to the lowest temperature at $\mu_0 H \geq 3$ T, around which a peculiar nFL behavior with reduced effective mass emerges. On the other hand, the application of high pressure induces complex evolution of magnetic states and realizes an AF quantum critical point around $P_c \approx 9$ GPa. Although we observed hallmarks of magnetic quantum criticality near P_c, no superconductivity was observed down to 2 K.

Acknowledgments

This work is supported by the National Key R&D Program of China (Grant Nos. 2018YFA0305700 and 2018YFA0305800), the National Natural Science Foundation of China (Grant Nos. 11888101, 11574377, 11834016, 11874400), the Strategic Priority Research Program and Key Research Program of Frontier Sciences of the Chinese Academy of Sciences (Grant Nos. XDB25000000, and QYZDB-SSW-SLH013). A portion of this research used resources at the High Flux Isotope Reactor, a DOE Office of Science User Facility operated by the Oak Ridge National Laboratory. MAM, JQY and BCS were supported at the Oak Ridge National Laboratory by the US Department of Energy, Office of Science, Basic Energy Sciences, Materials Sciences and Engineering Division Y.Y.J. and J.P.S. acknowledge support from the China Postdoctoral Science Foundation and the Postdoctoral Innovative Talent program.

Reference

1 G. Brostigen and A. Kjekshus, Acta Chem. Scand. **24**, 1925 (1970).

2 H. Holseth and A. Kjekshus, J. Less. Comm. Metal. **16**, 472 (1968).

3 E. E. Havinga, H. Damsma, and P. Hokkeling, J. Less. Comm. Metal. **27**, 169 (1972).

4 J. D. Donaldson, A. Kjekshus, D. G. Nicholson, and T. Rakke, J. Less. Comm. Metal. **41**, 255 (1975).

5 P. J. Sun, M. Søndergaard, B. B. Iversen, and F. Steglich, Ann. Phys. (Berlin) **523**, 312 (2011).

6 B. C. Sales, A. F. May, M. A. McGuire, M. B. Stone, D. J. Singh, and D. Mandrus, Phys. Rev. B **86**, 235136 (2012).

7 C. C. Homes, Q. Du, and C. Petrovic, Sci. Rep. **8**, 11692 (2018).

8 P. Sun, N. Oeschler, S. Johnsen, B. B. Iversen, and F. Steglich, Phys. Rev. B **79**, 153308 (2009).

9 N. Lazarević, M. M. Radonjić, R. Hu, D. Tanasković, C. Petrovic, and Z. V. Popović, J. Phys.: Conden. Matter **24**, 135402 (2012).

[10] H. Takizawa, M. Shimada, Y. Sato, and T. Endo, Mater. Lett. **18**, 11 (1993).
[11] H. Takizawa, K. Uheda, and T. Endo, J. Alloy. Comp. **287**, 145 (1999).
[12] P. Rhodes and E. P. Wohlfarth, Proc. Roy. Soc. London **273**, 247 (1963).
[13] E. P. Wohlfarth, J. Mag. Mag. Mater. **7**, 113 (1978).
[14] P. Shahi, et al., Phys. Rev. X **8**, 021055 (2018).
[15] J.-G. Cheng, K. Matsubayashi, S. Nagasaki, A. Hisada, T. Hirayama, M. Hedo, H. Kagi, and Y. Uwatoko, Rev. Sci. Instrum. **85**, 093907 (2014).
[16] R. Jaramillo, Y. Feng, J. Wang, and T. F. Rosenbaum, PNAS **107**, 13631 (2010).
[17] E. E. J. Huber and H. D. Ridgley, Phys. Rev. **135**, A1033 (1964).
[18] A. S. Wills, Physica B **276-278**, 680 (2000).
[19] M. B. Stone, M. D. Lumsden, S. E. Nagler, D. J. Singh, J. He, B. C. Sales, and D. Mandrus, Phys. Rev. Lett. **108**, 167202 (2012).
[20] T. Komatsubara, S. Shinohara, T. Suzuki, and E. Hirahara, J. Appl. Phys. **40**, 1037 (1969).
[21] T. Komatsubara, T. Suzuki, and E. Hirahara, J. Phys. Soc. Jpn. **28**, 317 (1970).
[22] A. Yeh, Y.-A. Soh, J. Brooke, G. Aeppli, T. F. Rosenbaum, and S. M. Hayden, Nature **419**, 459 (2002).
[23] P. Gegenwart, Q. Si, and F. Steglich, Nature Phys. **4**, 186 (2008).
[24] W. Wu, J.-G. Cheng, K. Matsubayashi, P. P. Kong, F. K. Lin, C. Q. Jin, N. L. Wang, Y. Uwatoko, and J. L. Luo, Nat. Comm. **5**, 5508 (2014).
[25] J.-G. Cheng, K. Matsubayashi, W. Wu, J. P. Sun, F. K. Lin, J. L. Luo, and Y. Uwatoko, Phys. Rev. Lett. **114**, 117001 (2015).

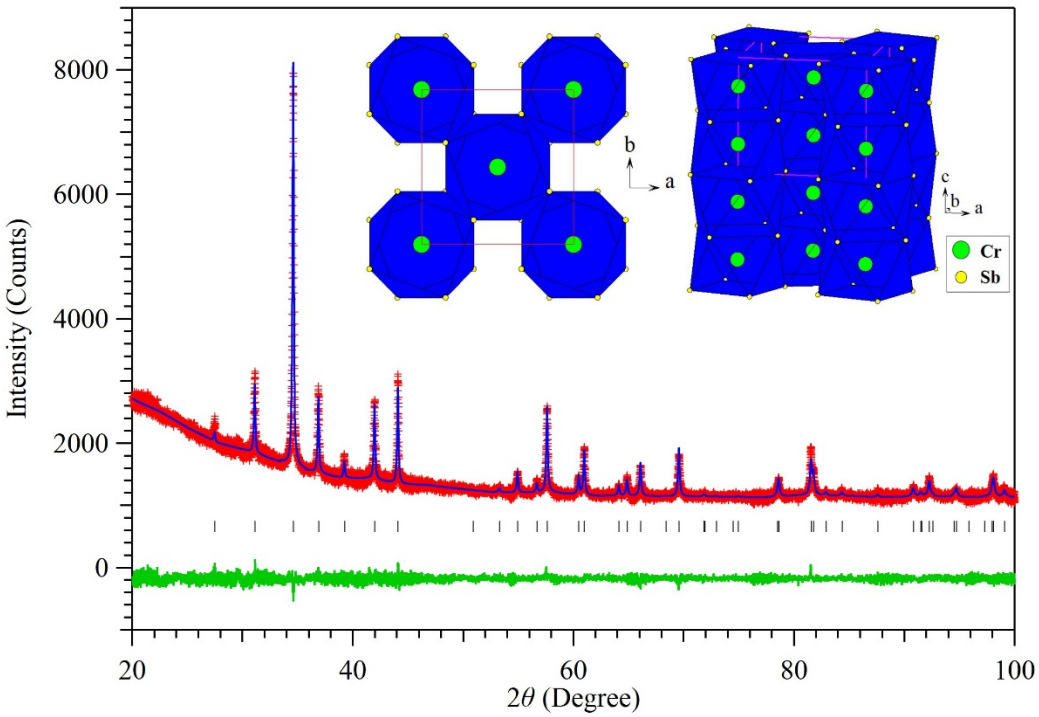

Fig. 1 Observed (cross), calculated (solid line), difference (bottom line) profiles of the powder XRD patterns of the high-pressure form of $CrSb_2$ after Rietveld refinements. The inset shows the crystal structures viewed along different directions.

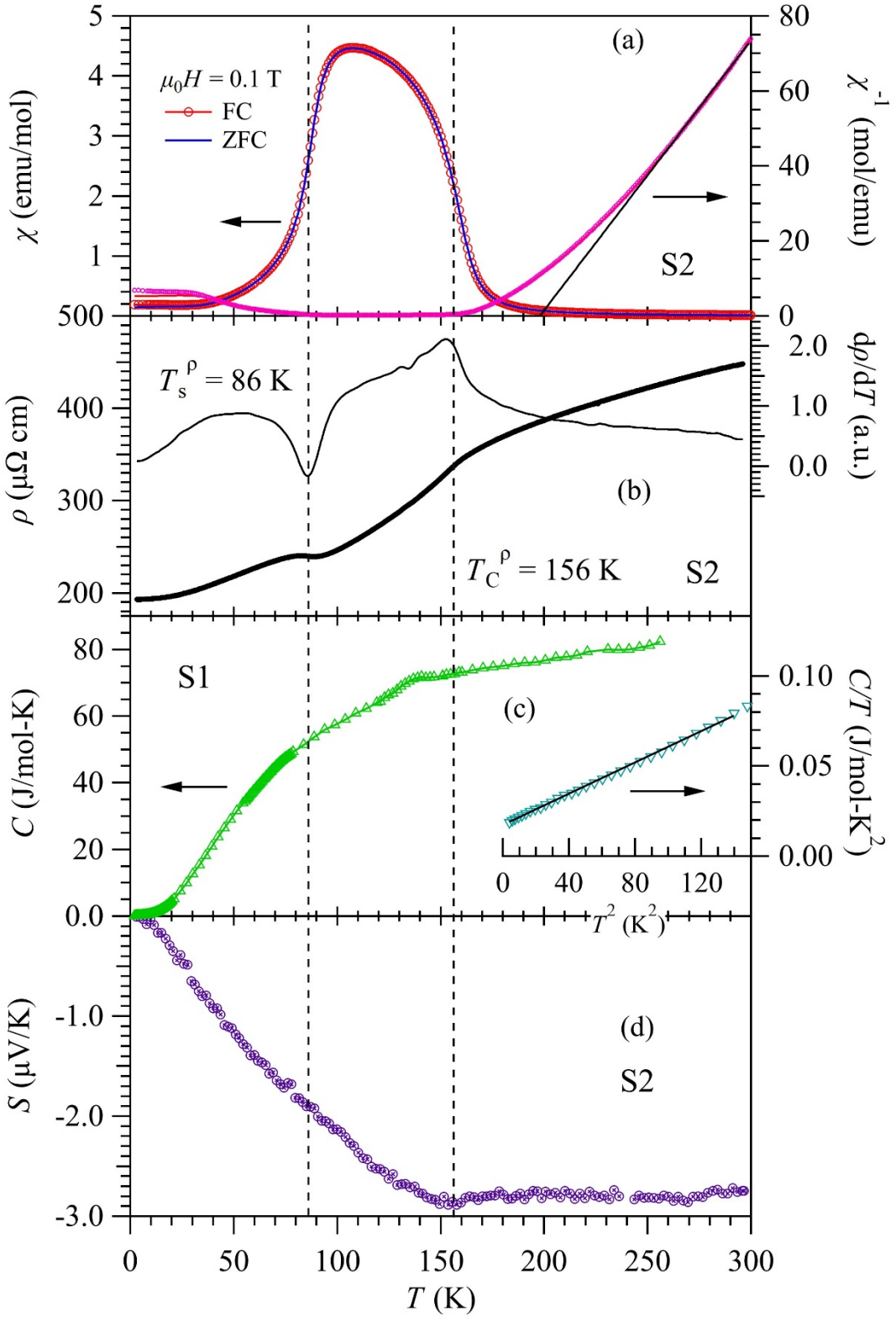

Fig. 2 Physical properties of high-pressure phase of $CrSb_2$. Temperature dependence of (a) magnetic susceptibility $\chi(T)$ and its inverse, (b) resistivity $\rho(T)$ and its derivative, (c) specific heat $C(T)$, and (d) thermopower $S(T)$ in the whole temperature range 2-300 K. Two magnetic transitions are marked by the vertical broken lines.

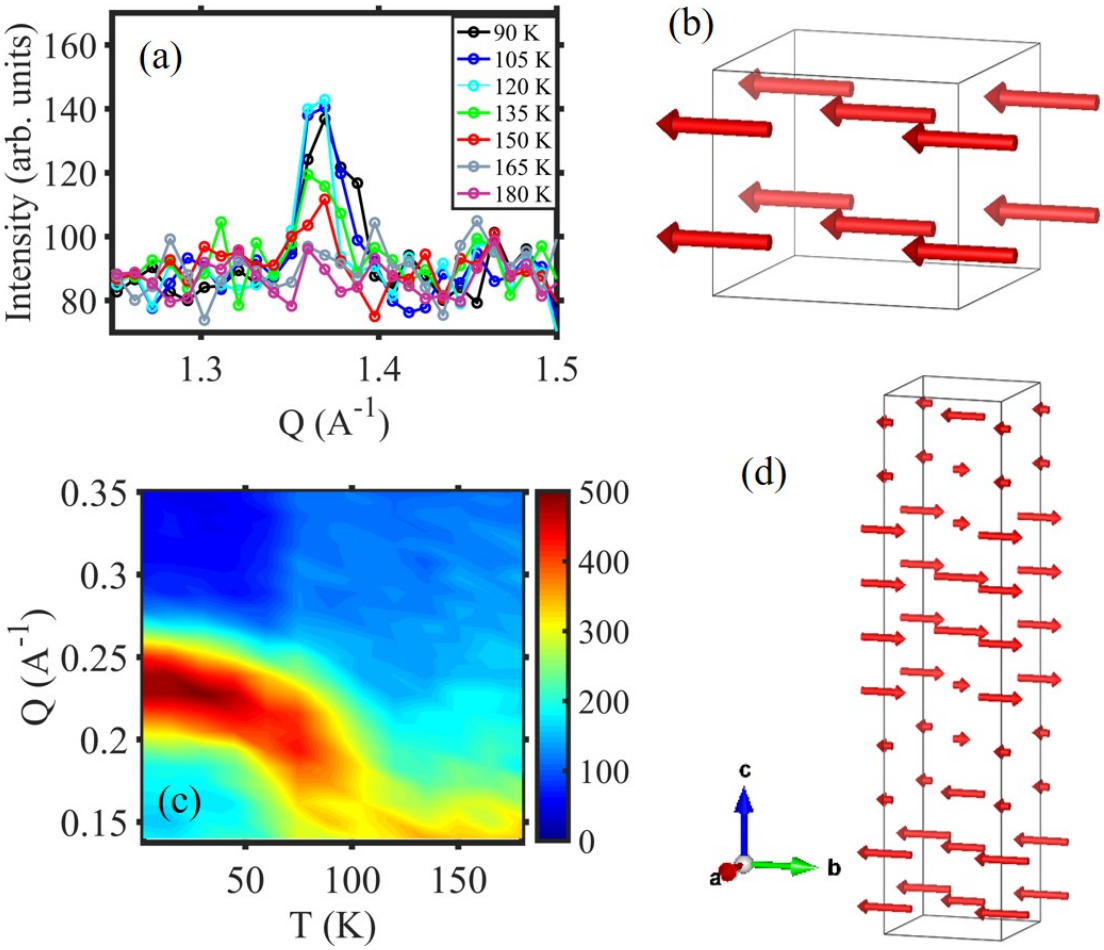

Fig. 3 Determination of the magnetic structure of $CrSb_2$ using neutron powder diffraction. (a) A magnetic reflection develops around 160 K. (b) This can be described by ferromagnetic ordering with moments in the ab-plane. (c) Below 120 K a low-angle reflection is observed that alters position with temperature. (d) The low temperature magnetic structure is determined to be a spin density wave with a propagation vector that alters with temperature. The case for k = (0,0,1/5) is shown.

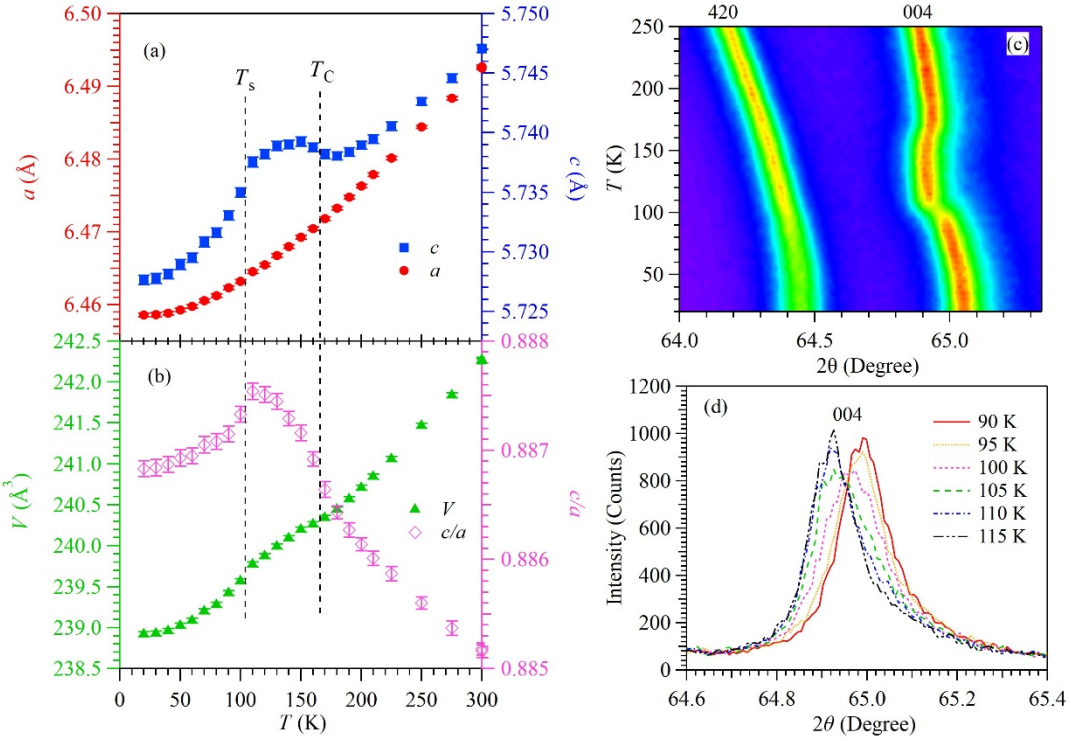

Fig. 4 (a, b) Temperature dependence of lattice parameters *a*, *c*, volume *V*, and *c/a* ratio. (c) Intensity maps of the 420 and 004 Bragg peaks. (d) Variation of the 004 peak position as a function of temperature.

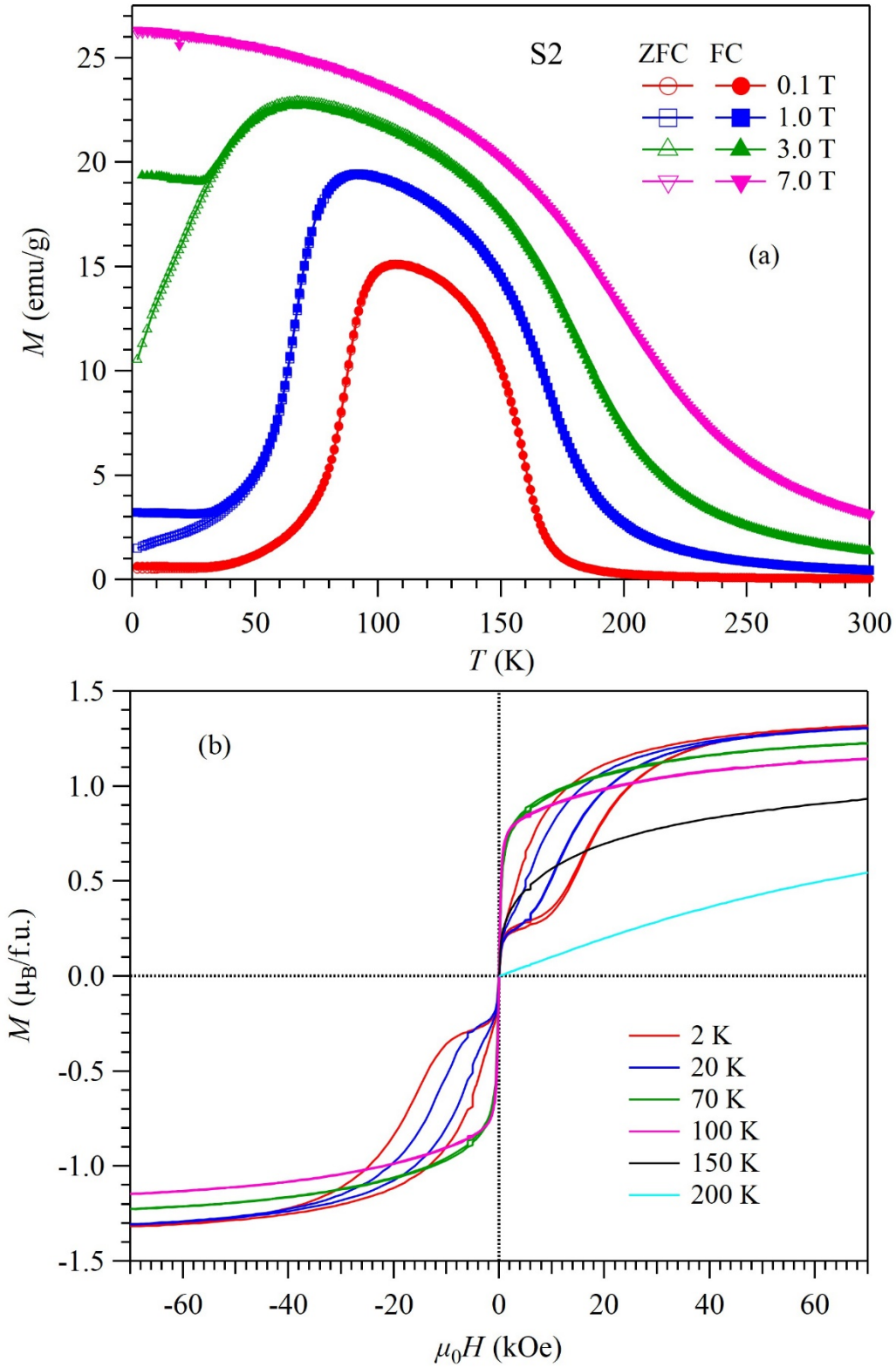

Fig. 5 (a) Temperature dependence of magnetization $M(T)$ for $CrSb_2$ measured under different magnetic fields up to 7 T in both zero-field-cooled (ZFC) and field-cooled (FC) modes. (b) Isothermal magnetization curves $M(H)$ between +7 and -7 T at different temperatures.

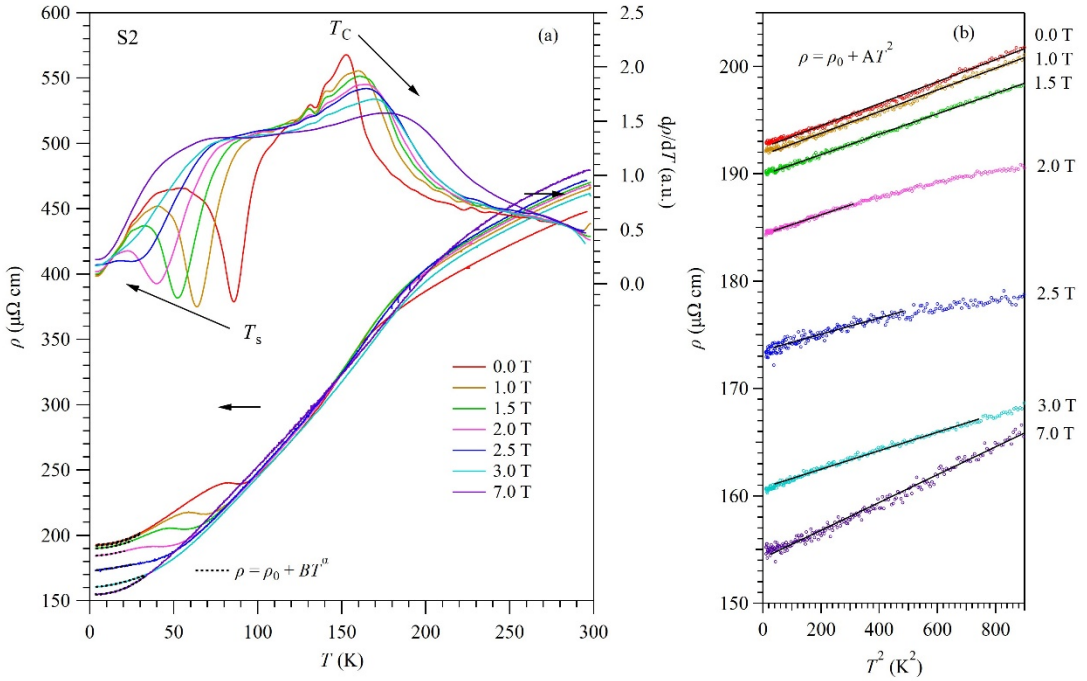

Fig. 6 (a) Temperature dependence of resistivity $\rho(T)$ of $CrSb_2$ measured under different magnetic fields up to 7 T. The magnetic transition temperatures T_C and T_s are determined from the peaks of dρ/dT curves shown on the top part of (a). (b) ρ vs T^2 plot of the low-temperature resistivity data.

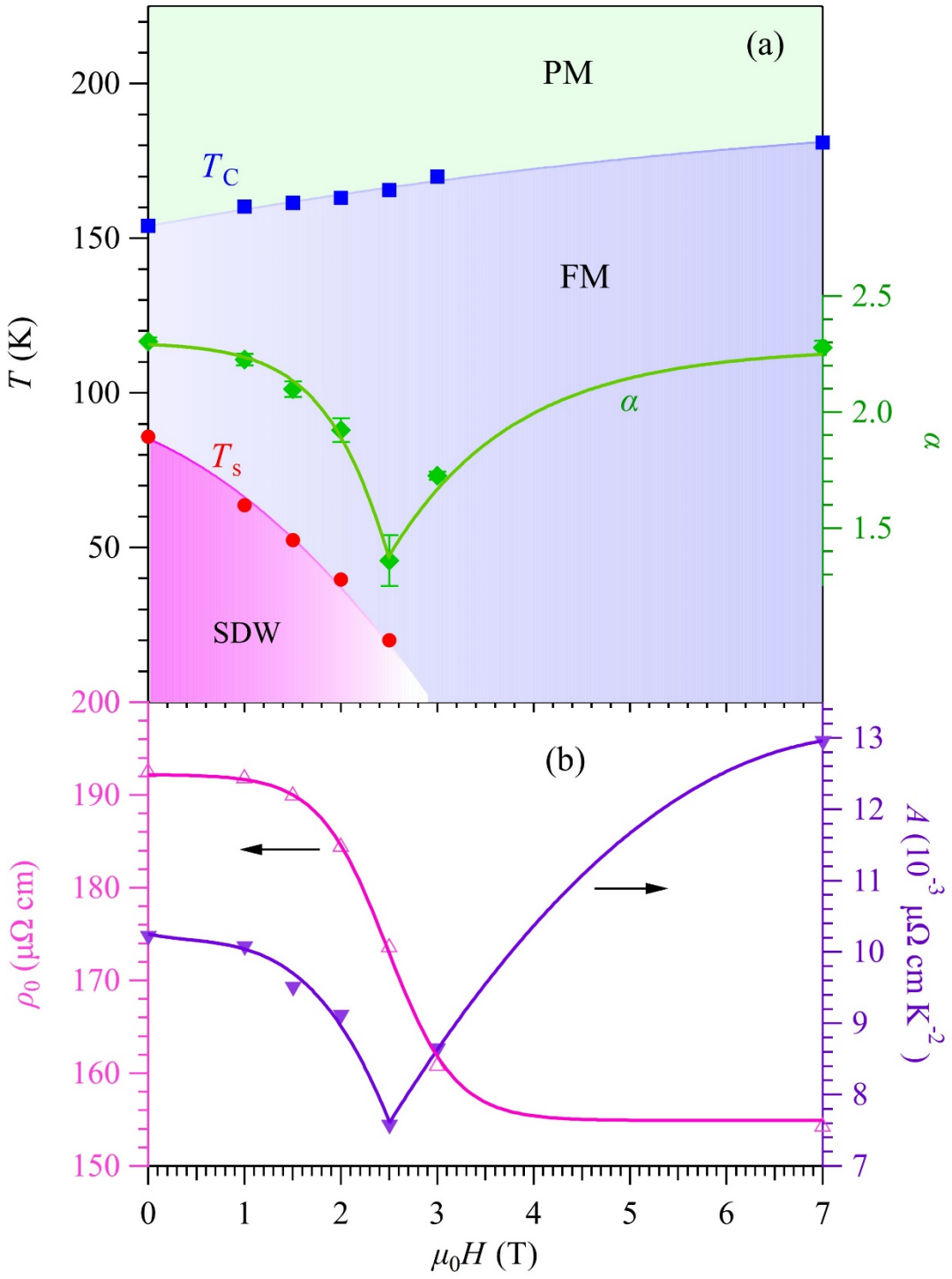

Fig. 7 Temperature-field phase diagram of $CrSb_2$. Field dependence of (a) T_C, T_s, and α, and (b) residual resistivity ρ_0 and T-quadratic coefficient A.

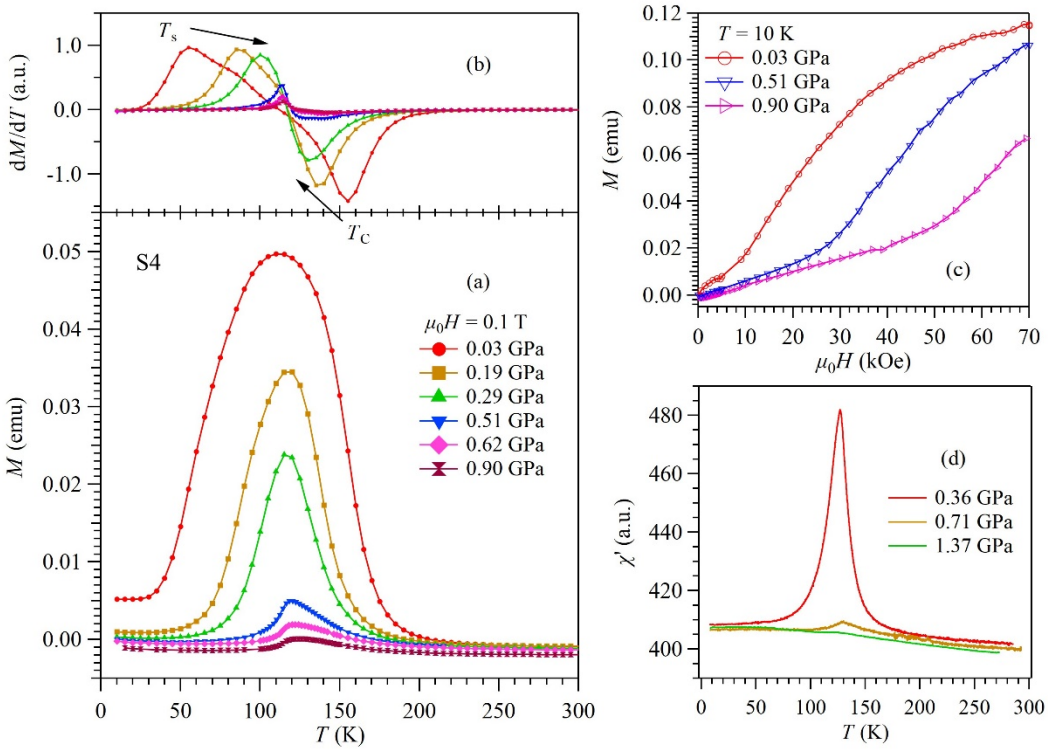

Fig. 8 Temperature dependence of (a) dc magnetization $M(T)$ and (b) its derivative dM/dT under various hydrostatic pressures up to 0.9 GPa measured with the piston-cylinder cell in MPMS. (c) Field dependence of dc magnetization $M(H)$ measured at 10 K for different pressures. (d) Temperature dependence of ac magnetic susceptibility $\chi'(T)$ under different hydrostatic pressures measured with a piston-cylinder cell.

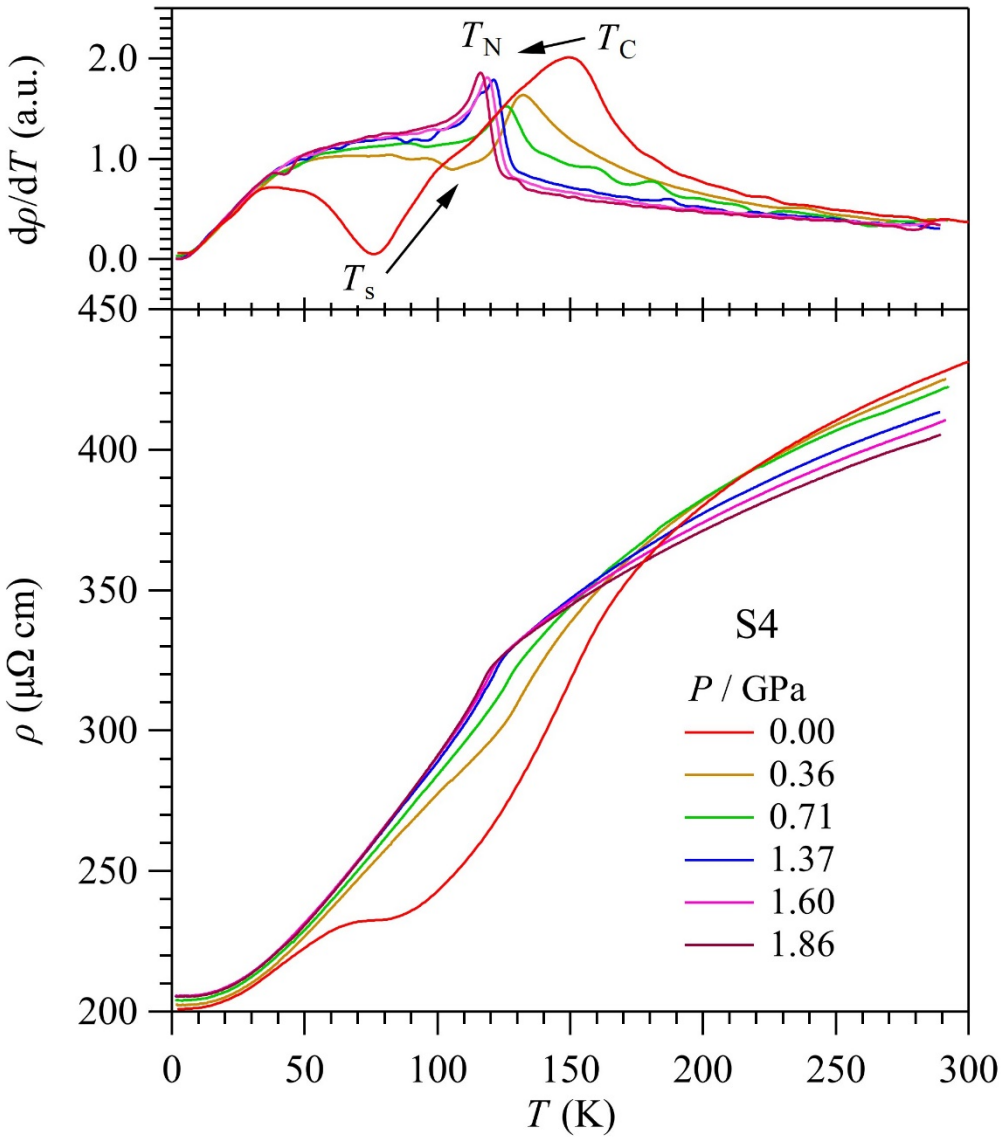

Fig. 9 Temperature dependence of resistivity $\rho(T)$ of $CrSb_2$ under various hydrostatic pressures up to 1.86 GPa measured with a self-clamped piston-cylinder cell. The top panel shows the temperature derivative curves dρ/dT.

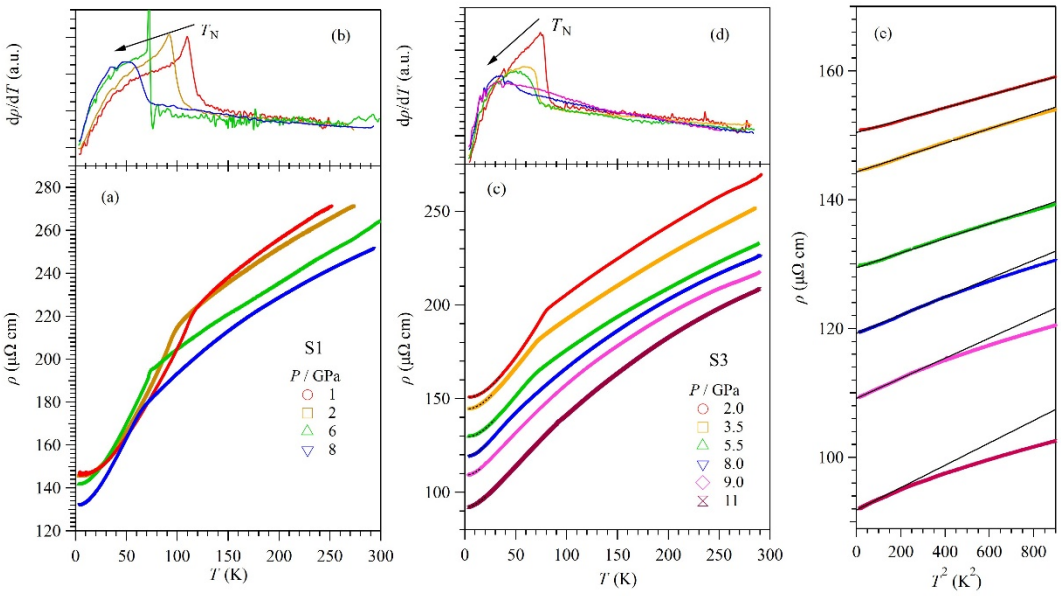

Fig. 10 Temperature dependence of resistivity $\rho(T)$ and its derivative $d\rho/dT$ of $CrSb_2$ under various hydrostatic pressures up to 8 GPa (a, b), and up to 11 GPa (c, d), measured with a palm cubic anvil cell. The top panels show the temperature derivative curves $d\rho/dT$. (e) ρ vs T^2 plot of the low-temperature resistivity data of S3 sample.

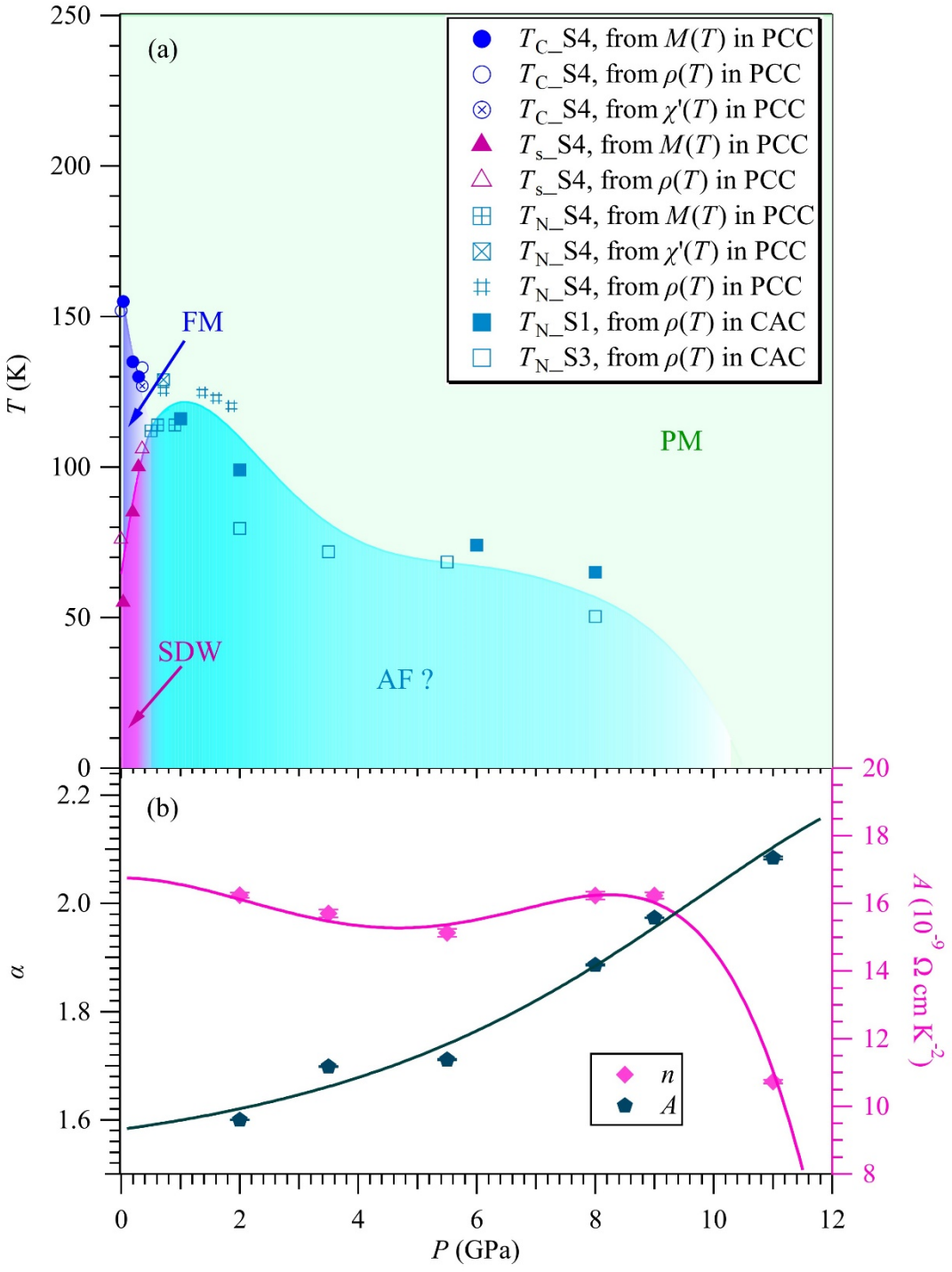

Fig. 11 (a) Temperature-pressure phase diagram of $CrSb_2$. (b) Pressure dependences of the resistivity exponent α and the T-quadratic coefficient A.

Supplemental Materials

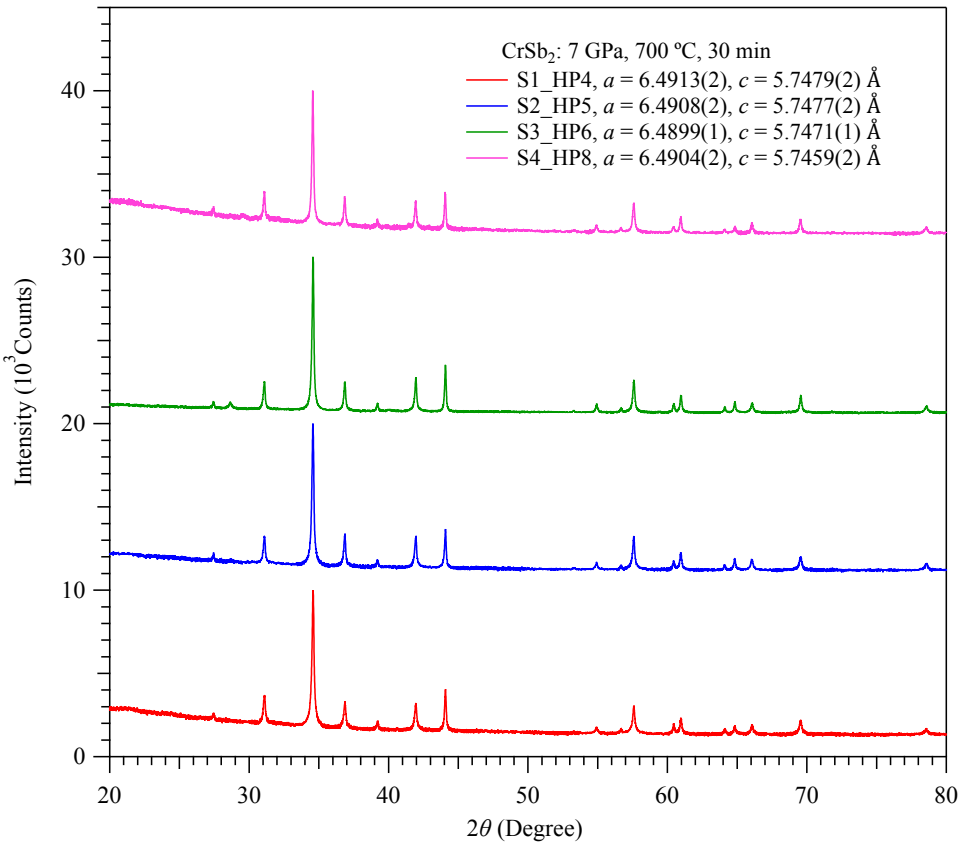

Fig. S1 Powder XRD patterns of four $CrSb_2$ samples (S1 to S4) prepared under similar conditions. The lattice parameters are given inside the figure.

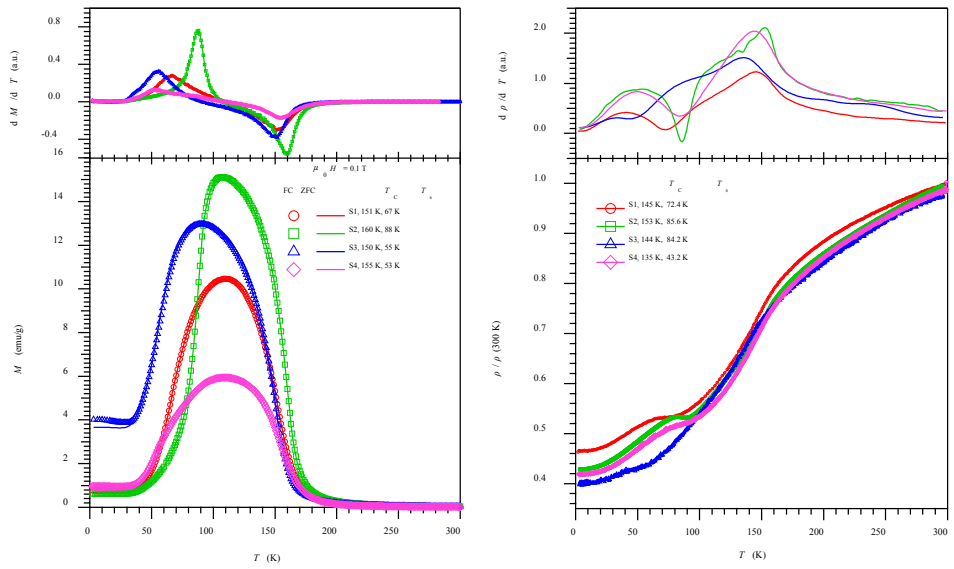

Fig. S2 Temperature dependence of (left) magnetization $M(T)$ and (right) resistivity $\rho(T)$ for the four samples. The two magnetic transitions, T_C and T_s, determined from the temperature derivative are listed inside the figures. As can be seen, although the features are very similar, these two transition temperatures are sample dependent.